

Pinhole interferometry with coherent hard X-rays

Wolfram Leitenberger,^{a*} Horst Wendrock,^b
Lothar Bischoff^c and Timm Weitkamp^d

^aUniversität Potsdam, Institut für Physik, Am Neuen Palais 10, D-14469 Potsdam, Germany, ^bInstitut für Festkörper- und Werkstofforschung, POB 270016, D-01171 Dresden, Germany, ^cForschungszentrum Rossendorf eV, POB 510119, D-01314 Dresden, Germany, and ^dPaul-Scherrer-Institut, CH-5232 Villigen, Switzerland. E-mail: leitenberger@rz.uni-potsdam.de

This paper discusses the experimental realisation of two types of X-ray interferometer based on pinhole diffraction. In both interferometers the beam splitter was a thin metal foil containing micrometer pinholes to divide the incident X-ray wave into two coherent waves. The interference pattern was studied using an energy-dispersive detector to simultaneously investigate in a large spectral range the diffraction properties of the white synchrotron radiation. For a highly absorbing pinhole mask the interference fringes from the classical Young's double-pinhole experiment were recorded and the degree of coherence of X-rays could be determined. In the case of low absorption of the metal foil at higher X-ray energies (>15 keV) the interference pattern of a point diffraction interferometer was observed using the same set-up. The spectral refraction index of the metal foil was determined.

Keywords: coherent X-rays; double-slit interferometer; point diffraction interferometer; refraction index; white synchrotron beam.

1. Introduction

The double-pinhole (double-slit) interferometer (DPI) (Young, 1807; Thompson & Wolf, 1957) and the point diffraction interferometer (PDI) (Linnik, 1933; Smartt & Steel, 1975) are both standard types of interferometers and first used with visible light. Recently, several authors used a DPI at short wavelengths in the EUV (Chang *et al.*, 2000), soft X-ray (Ditmire *et al.*, 1996; Takayama *et al.*, 1998; Burge *et al.*, 1999; Liu *et al.*, 2001; Paterson *et al.*, 2001) and hard X-ray (Leitenberger *et al.*, 2001) regions. In a DPI, two coherently illuminated tiny pinholes of the same size generate two spherical wavefronts by diffraction. The evaluation of the interference pattern is widely used for characterization of the coherence properties of the incident radiation. In a PDI, a spherical reference wavefront generated by diffraction from a tiny pinhole interferes with the wavefront transmitted through the membrane containing the pinhole itself. This type of interferometer is also used with short-wavelength EUV radiation for testing of wavefronts of optical components (Goldberg *et al.*, 1995; Naulleau & Goldberg, 1999) or for the measurement of the refraction index of the transparent membrane.

In this paper we describe experiments using both types of interferometers, with X-rays of energies from 5 to 20 keV. The experiments were performed using white synchrotron radiation at the EDR beamline, dedicated to energy-dispersive reflectometry at the BESSY II synchrotron in Berlin, Germany (Neissendorfer *et al.*, 1999; Bodenthin *et al.*, 2002).

A quantitative characterization of the coherence properties of hard X-rays has already been demonstrated by several groups using different interferometric methods (Ishikawa, 1988; Lang & Make-

peace, 1999; Kohn *et al.*, 2000; Leitenberger *et al.*, 2001; Lengeler, 2001; Yabashi *et al.*, 2001). Knowledge of the coherence properties is important for several applications with coherent radiation in X-ray optics, imaging, speckle correlation spectroscopy or holography (Snigirev, Snigireva *et al.*, 1996; Cloetens *et al.*, 1996; Snigirev, Kohn *et al.*, 1996; Wilkins *et al.*, 1996; Leitenberger *et al.*, 2000; Leitenberger & Snigirev, 2001; Lengeler *et al.*, 2001). For this reason a simple experimental method is of great interest for routine measurements.

The initial aim of the experiments was the quantitative determination of the spatial coherence of synchrotron radiation in the hard X-ray region by performing Young's double-slit experiment. It should be possible to perform these measurements even with white synchrotron radiation in a large spectral range from 5 to 20 keV (0.6 to 2.5 Å wavelength) using a detector with a comparably low energy resolution which is identical to a very small longitudinal coherence length (Leitenberger *et al.*, 2003). Under ambient conditions, radiation energies below 5 keV were not accessible owing to strong absorption in air, and for X-rays above 20 keV the emitted intensity of the bending magnet is already quite low.

Tiny pinholes in a tantalum membrane are the key elements of the experiment. They were fabricated by the focused ion-beam technique (FIB) as proposed by Walker *et al.* (1996) and David *et al.* (2000). In our case the thickness of the tantalum foil was limited to 30 µm owing to technical reasons (see below). The absorption coefficient of the tantalum foil strongly depends on the energy of the incident radiation. For low energies it is opaque and for high energies it is more or less transparent. For this reason one can distinguish two different modes of operation of the pinhole mask in one set-up: (i) a double-pinhole interferometer (DPI) for high absorption, and (ii) a point diffraction interferometer (PDI) for low absorption.

1.1. Fabrication and characterization of the micropinholes

For the generation of the microstructures a focused ion-beam system [FIB200 (FEI)] was used. This system uses a beam of Ga⁺ ions with an energy of 30 kV which can be focused down to a spot of diameter 8 nm. The ion optics allows the beam to scan with a nm resolution over a small sample area and generates any pixel pattern on the surface of the target. The current of the ion beam can be chosen to be between 1 pA and 11 nA. With low beam current the smallest point size is available.

During the bombardment of the target with gallium ions a small amount of material was removed from the surface. For a tantalum target a value of 0.26 µm³ nC⁻¹ was determined. The secondary electrons emitted in parallel can be collected similarly to a conventional SEM with an electron detector and the progress of the sputtering process can be observed. For the generation of circular microholes a pixel file of a circle was generated which was transferred to the target. Because the metal removal becomes lower with increasing depth of the hole, a smaller hole having a tenth of the final hole diameter was generated first in order to achieve a breakthrough of the ion beam. After this the material removal was much faster. The beam current through the sample was measured during the sputtering process in order to determine when the breakthrough of a hole was reached. Using a 2700 pA beam current it finally took about 1 h to sputter one 4 µm pinhole into the 30 µm tantalum foil.

As seen from the FIB-SE images (Fig. 1), the inner surface of the pinhole and the borders are very smooth. The holes have an almost elliptical form which varies slightly for each pinhole. The influence of the non-uniform size of the two pinholes on the diffraction pattern was investigated by numerical simulations. The calculated fringe

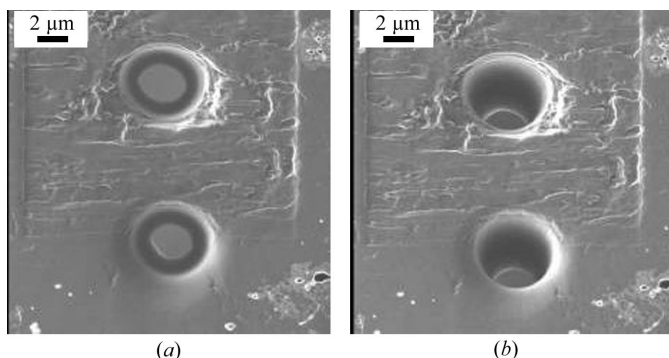


Figure 1
FIB-SE images with ion-induced secondary electrons of the two micropinholes in a 30 μm tantalum foil. The diameter is 2 μm and the separation is 11 μm . (a) Top view. (b) Tilted by 10°.

visibility was almost unaffected after changing the shape and the diameter of the pinholes by 10%.

1.2. Numerical simulation

As discussed in detail below, the diffraction experiments were performed under ‘near-field’ conditions where a simple analytical description of the diffraction pattern does not exist. In order to interpret the experimental diffraction pattern and to obtain quantitative information from that data, we performed numerical simulations of the interference pattern using Fresnel propagation in paraxial approximation (Goodman, 1968). The propagation was carried out in Fourier space, and optical materials constants were taken from the CXRO database (Henke *et al.*, 1993). A more detailed description of the code can be found elsewhere (Weitkamp, 2002; Weitkamp *et al.*, 2002). Since the double pinhole is a two-dimensional pattern and distinctly different from the one-dimensional case of a double slit, all calculations were carried out in two dimensions, even those where only section profiles through the images are used. The wavefront array for the simulations contained 1024×1024 square pixels of size $0.5 \mu\text{m} \times 0.5 \mu\text{m}$. For Figs. 6 and 7, where diffraction images at different photon energies are simulated, the incident intensity was scaled with the emission spectrum of a BESSY bending magnet, calculated with the aid of a web-interfaced program by the Center of X-ray Optics at the ALS in Berkeley (http://www-cxro.lbl.gov/optical_constants/).

2. Experiment

The measurements were performed at a bending-magnet beamline providing a white synchrotron beam. A sketch of the experimental set-up and the working principle of both types of interferometers are shown in Fig. 2. In between the X-ray source and the experimental area the only solid matter in the beam path were two beryllium vacuum windows and four 50 μm -thick capton foils. The tantalum membrane with the pinholes was adjusted on a goniometer under ambient conditions. The illuminated spot on the Ta foil was defined to $500 \mu\text{m} \times 500 \mu\text{m}$ by the entrance slit behind the vacuum exit window. In this way the background intensity was reduced. The slit size was not reduced in order to prevent an unequal illumination of the two pinholes owing to additional slit diffraction.

The lateral intensity distribution of the diffraction pattern was recorded by scanning a small pinhole on a remote-controlled high-precision translation stage in front of the detector. In order to reduce the absorption of the radiation in air we put a tube filled with helium

in between the double pinhole and the detector. The total path length of the radiation in air was reduced to about 70 cm.

The energy resolution of the detector [based on a silicon drift chamber (Röntec)] is about 200 eV in the energy range from 2 to 40 keV. The whole spectrum is divided into 4096 channels. For data evaluation, eight neighboring channels were summed to decrease the noise without losing energy resolution. During the experiments the beam current in the storage ring was about 200 mA. The typical count rate of the detector at maximum intensity was $150\,000 \text{ counts s}^{-1}$ over the whole spectral range and a typical measuring time per data point was 10 s. A pinhole of diameter 5 μm was the smallest available detector pinhole. Its effective height was halved to 2.5 μm by adjusting a horizontal metal blade just behind the pinhole. In the following experiments the lateral resolution for vertical detector scans was 2.5 μm and that for horizontal scans was 5 μm . By reduction of the count rate the ‘dead-time effects’ of the detector electronics could be reduced.

2.1. Conditions for a DPI

The intensity distribution $I(x)$ behind a double pinhole in the far-field can be written as

$$I(x) = I_0 \left[\frac{J_1(k_d x)}{k_d x} \right]^2 [1 + V \cos(k_D x)] + I_b, \quad (1)$$

with

$$k_d = 2\pi d/\lambda L \quad \text{and} \quad k_D = 2\pi D/\lambda L.$$

For uniform illumination of both pinholes the modulus of the complex coherence factor is equal to the fringe visibility (fringe contrast) V ,

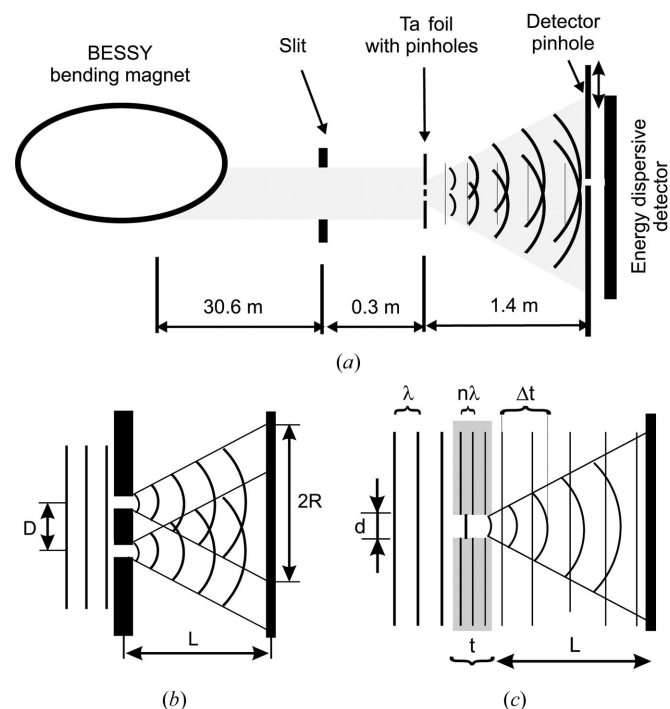


Figure 2
Experimental set-up with symbolic representation of propagating waves. (a) Schematic view of the beamline set-up. (b) Double-pinhole interferometer. (c) Point diffraction interferometer.

$$V = \frac{I_{\max} - I_{\min}}{I_{\max} + I_{\min}} = \frac{\sin(\pi s D / \lambda L)}{\pi s D / \lambda L} \quad (2)$$

The variables are as follows: x , coordinate in the diffraction plane (both parallel to the pinhole separation); d , diameter of an individual pinhole; D , pinhole separation; L , pinhole-to-detector distance; λ , wavelength; J_1 , modified Bessel function of the first kind describing the pinhole diffraction; z , source-to-pinhole distance; s , size of the X-ray source; I_{\max} and I_{\min} are the maximum and the minimum intensities around a central peak and I_b takes into account a constant background (Francon, 1966; Born & Wolf, 1999).

Owing to limited space in the experimental hutch the maximum distance between the double pinhole and the detector was $L_{\text{exp}} = 1.40$ m. This is a relatively small distance for the small diffraction angles occurring at this short wavelength. To observe interference of both diffracted waves they must sufficiently overlap each other after propagation from the pinholes to the detector. The width of the first diffraction minimum $2R$ in the distance L behind a pinhole of diameter d at a wavelength λ is given by the Airy criterion, $2R = 1.22L\lambda/d$. The degree of overlap, O , can be expressed as

$$O = 1 - \frac{D}{2R} = 1 - \frac{Dd}{1.22L\lambda} \quad (3)$$

(see Fig. 2). A complete overlap of the diffraction maxima of $O \approx 1$ is reached for very large values of L . Let us assume an overlap of at least 0.8 to obtain an evaluable interference pattern from the experiment. With the experimental parameters $d = 2 \mu\text{m}$, $D = 11 \mu\text{m}$, $L = 1.40$ m and $\lambda = 1 \text{ \AA}$, we obtain $O = 0.87 > 0.8$, and we can expect an interference pattern. A weaker interference effect is expected for the next example: $d = 2 \mu\text{m}$, $D = 37 \mu\text{m}$ and $\lambda = 1 \text{ \AA}$ gives $O = 0.57 < 0.8$. Some examples calculated according to equation (3) are shown in Fig. 3(a). We can conclude that owing to the small detector distance in the experiment we cannot expect an evaluable interference pattern at a large pinhole distance and higher energies by using equation (1).

Next we consider the validity of the Fraunhofer criterion for our experimental set-up. A quantitative investigation of the problem can be found by Garcia-Sucerquia *et al.* (2001). The expression $\Delta^2/\lambda \ll L$ gives a minimum distance L for which the theoretical description of so-called 'far-field diffraction' can be applied for diffraction at objects with largest extension Δ . For observation of maximum interference contrast in the diffraction pattern the detector distance should be very large. Fig. 3(b) shows the minimum detector distances L for some Δ values calculated for the energy range used in the experiment. For example, with objects smaller than $10 \mu\text{m}$ the far-field condition is valid up to 17 keV radiation. At higher energies and larger objects the near-field or Fresnel diffraction theory has to be applied for comparing experiment with calculations according to equation (1). From the calculations one can conclude that the far-field condition for the DPI case is much more difficult to realise than for the PDI case because in the first case Δ is identical to the pinhole separation whereas in the second case Δ is equivalent to the pinhole diameter.

In the following we use the description of the X-rays by energy and wavelength in parallel. The conversion from the energy to wavelength description is achieved using $\lambda = hc/E = 12.398/E$, where h is Planck's constant, c is the speed of light, and with energy E in keV and wavelength λ in \AA .

3. Results and discussion

During the measurements of the intensity distribution in the diffraction pattern the whole energy spectrum is recorded at each position of the detector pinhole. The calculated energy spectrum

without consideration of the small pinholes in the Ta foil is shown in Fig. 4. The intensity of the originally emitted white synchrotron beam decreases by more than two decades within the observed energy interval. A big part of the white beam is absorbed by different media of thickness t in the beam path: beryllium windows ($t = 500 \mu\text{m}$), air ($t = 0.7$ m), helium ($t = 1.0$ m) and tantalum ($t = 30 \mu\text{m}$). The absorption is strongly energy dependent with highest absorption at low energies and just above the absorption edges of tantalum at 9.88 and 11.1 keV.

3.1. Line scan – pinhole separation $11 \mu\text{m}$

Using the double-pinhole mask shown in Fig. 1, the diffraction pattern was recorded by scanning the detector pinhole with a $1 \mu\text{m}$ step size in a direction perpendicular to the incident beam. Before we look in detail at the measured diffraction profiles for a single energy, which are extracted from a series of energy spectra, we will look at two energy spectra (Fig. 5). One spectrum was recorded on the optical axis which is defined by a straight line from the source to the

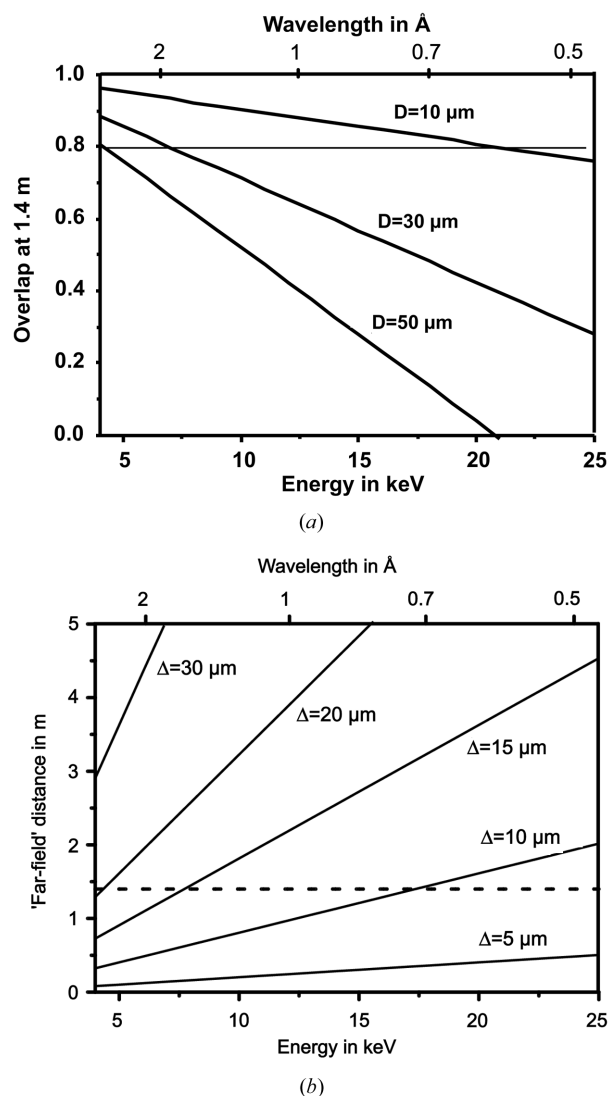


Figure 3 (a) Degree of overlap of the diffraction pattern of the two pinholes at 1.4 m behind the pinhole mask for different pinhole distances D according to equation (3). (b) Minimum distance for the so-called 'far-field diffraction' condition as a function of energy for different object sizes Δ . The dashed line signifies the detector distance in the present experiment.

middle between the two pinholes, and the other spectrum was recorded 200 μm off-axis. The off-axis spectrum qualitatively matches the calculated absorption spectrum of the 30 μm tantalum foil (Fig. 4). In the on-axis spectrum, much higher intensity is observed owing to pinhole diffraction. The small oscillations will be discussed in detail later. The value of the intensity ratio of the wave diffracted by the pinholes and the transmission through the foil, I_0/I_{200} , is important for the visibility of the interference effect in the PDI case. For large quotients (>10) one expects a good interference contrast for the DPI with small contributions of transmitted radiation, whereas small values around unity signify a strong contribution of the transmitted wave.

Fig. 6(a) shows in a greyscale map the raw data of the 141 energy spectra recorded at a distance of $\pm 70 \mu\text{m}$ from the optical axis. In this image one sees immediately the main properties of the pinhole interferometer over the whole energy range:

(i) The almost horizontally oriented dark bands are the maxima of Young's interference fringes of the DPI and their distance decreases with higher energy.

(ii) The half-circle-like pattern on the left-hand side of Fig. 6 is caused by interference of pinhole waves with the transmitted plane

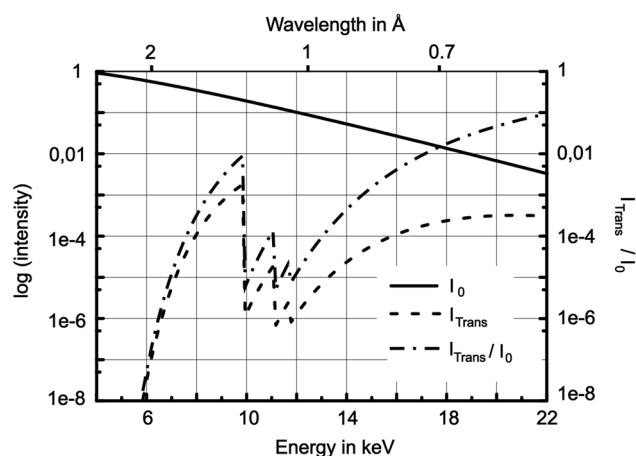


Figure 4 Calculated intensity distribution $I_0(E)$ of a bending magnet at BESSY and transmitted intensity $I_{\text{trans}} = I_0(1 - I_{\text{absorb}})$ after passing through 30 μm of tantalum and 70 cm of air. In addition, the ratio I_{trans}/I_0 giving the normalized transmission is shown.

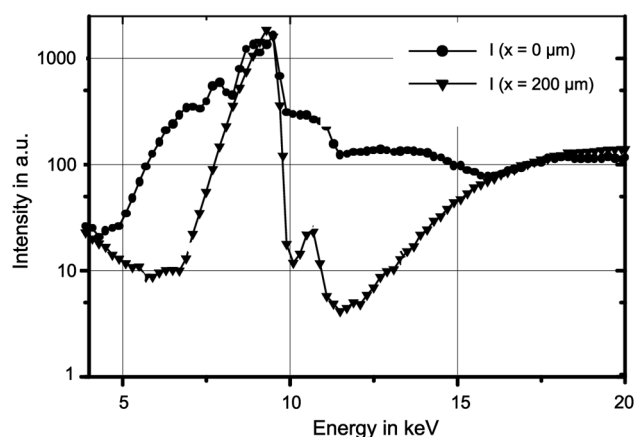


Figure 5 Spectral intensity distribution of the transmitted intensity measured with an energy-dispersive detector with a tiny pinhole in front. The two spectra were recorded on the optical axis and 200 μm off-axis.

wave (PDI). If the 'pinhole waves' and the transmitted plane waves are of comparable strength, their interference fringes become visible until high orders.

(iii) From about 16 keV to higher energies the maximum intensity is no longer in the center of the interference pattern. The measured diffraction profile is always a convolution of the diffraction profile with the detector slit and the size of the X-ray source (Kohn *et al.*, 2000). This is why, at certain energy values, inverted or even 'zero' contrast is observed.

(iv) The absorption edges of the tantalum foil are visible as vertical dark bands at around 9.9 and 11.1 keV.

Fig. 6(b) shows the result of calculations obtained using a wave-propagation technique using the same parameters as in the experiment: $d = 2.6 \pm 0.1 \mu\text{m}$, $D = 12.6 \pm 0.1 \mu\text{m}$, $L = 1.4 \text{ m}$. The values of d and D were calculated from the fit of equation (1) to the measured data for several energy values.

3.2. Line scan – pinhole separation 37 μm

The diffraction pattern in Fig. 7 measured for two pinholes separated vertically by $D = 37 \mu\text{m}$ differs from the previous one. From left to right one finds the following:

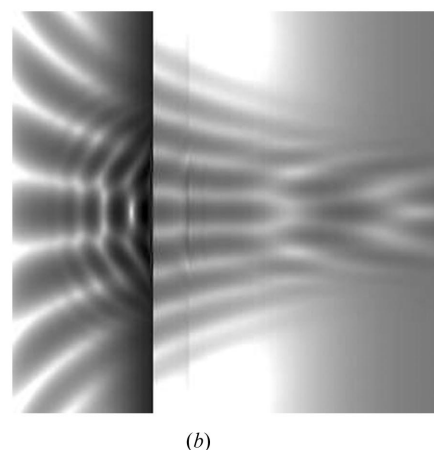
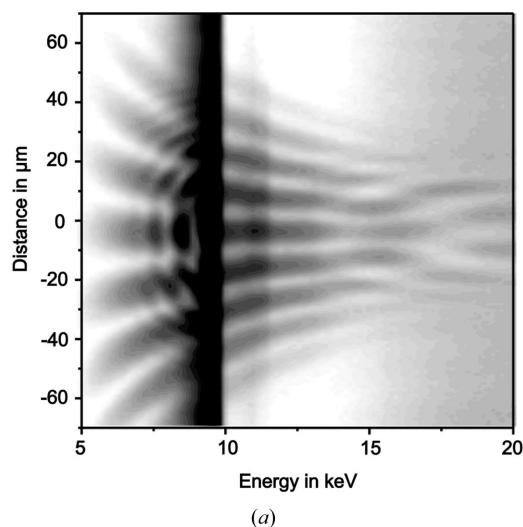


Figure 6 Diffraction pattern of two 11 μm -separated pinholes. In the range $x = \pm 70 \mu\text{m}$ around the optical axis, 141 energy spectra (5–20 keV) were recorded. In this plot, each horizontal line is an energy spectrum and black represents high intensity. (a) Experiment. (b) Simulation, same scaling as in (a).

(i) Young's fringes have a smaller distance and are only visible in the range 5–8 keV.

(ii) 'Half circles' from the PDI are clearly visible (8–9.9 keV).

(iii) Young's fringes disappear completely for energies larger than 13 keV and a parabola-like pattern with alternating contrast originated by the transmitted wave appear again.

Because of the larger distance between the two pinholes compared with the previous experiment they act more like two independent point sources. Especially at short-wavelength values both diffraction patterns do not overlap and Young's fringes are not visible ($E > 13$ keV). Another point is the short propagation distance of 1.4 m behind the double pinhole; this is the second reason why the waves do not overlap and no significant interference effects occur. Using equation (3) one obtains $O = 0.15$. The numerical simulation shown in Fig. 7(b) was performed using the parameters $d = 3.7 \pm 0.2 \mu\text{m}$ and $D = 37.0 \pm 0.3 \mu\text{m}$, which were calculated from the fit of equation (1) to the measured data for several distinct energy values.

3.3. Area map – pinhole separation 37 μm

A two-dimensional intensity map of the interference pattern of the two 37 μm -separated pinholes was obtained by scanning the detector pinhole vertically and horizontally. Fig. 8 shows a series of ten diffraction patterns at different beam energies. The values were extracted from the 900 recorded spectra. The step size was 2 μm

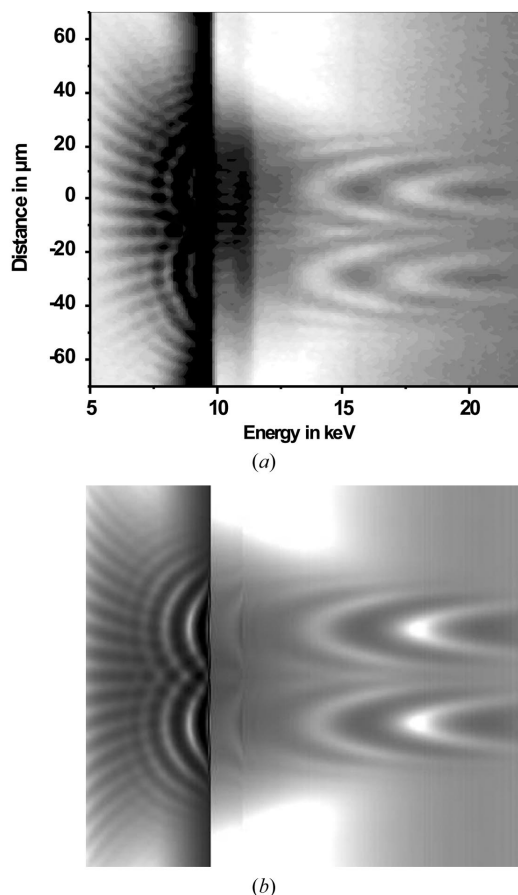


Figure 7
Diffraction pattern of two pinholes with a 37 μm separation. In the range $\pm 70 \mu\text{m}$ around the optical axis, 141 energy spectra (5–22 keV) were recorded. In this plot, each horizontal line is an energy spectrum and black represents high intensity. Below 8 keV, Young's fringes appear and above 10 keV the point diffraction interferograms of both pinholes are visible. (a) Experiment. (b) Simulation, same scaling as in (a).

vertically and 5 μm horizontally. The energy positions of the maps correspond to the energy values marked in Fig. 11. These maps nicely illustrate the results of the linear diffraction pattern already given in Figs. 6 and 7:

(i) For energies below 7 keV the almost unmodified 'zebra pattern' of Young's fringes is visible.

(ii) In the interval from 8 to 8.5 keV, Young fringes and the concentric 'PDI rings' are both visible, and until 9.9 keV Young's fringes disappear completely.

(iii) In between the absorption edge at 9.9 keV and about 13 keV Young's fringes appear again owing to higher absorption of the transmitted wave. The low fringe visibility is caused by the small detector distance and large source size.

(iv) Above 13 keV only the PDI pattern is visible. Here the alternating ring contrast for different energies is caused by the energy-dependent phase shift of the plane wave (see Fig. 11).

(v) Some values of the overlap parameter O are 0.61 (6 keV), 0.35 (10 keV) and 0.03 (16 keV). These are comparably low for the whole measured energy range.

The numerical simulations shown in Figs. 6(b) and 7(b) were performed using the same parameters as in the experiment and a source size of 40 μm . In general, sharper details of the PDI interference rings than in the experiments are shown. The Young's fringes at 10 and 11 keV are surprisingly more visible in the experiment than in the simulation. This might be caused by a value of the pinhole separation which is larger than that in the experiments. These small discrepancies were not investigated further.

3.4. Double-pinhole interferometer (DPI)

A quantitative evaluation of the interference pattern of the DPI was carried out by determination of the fringe visibility by fitting the

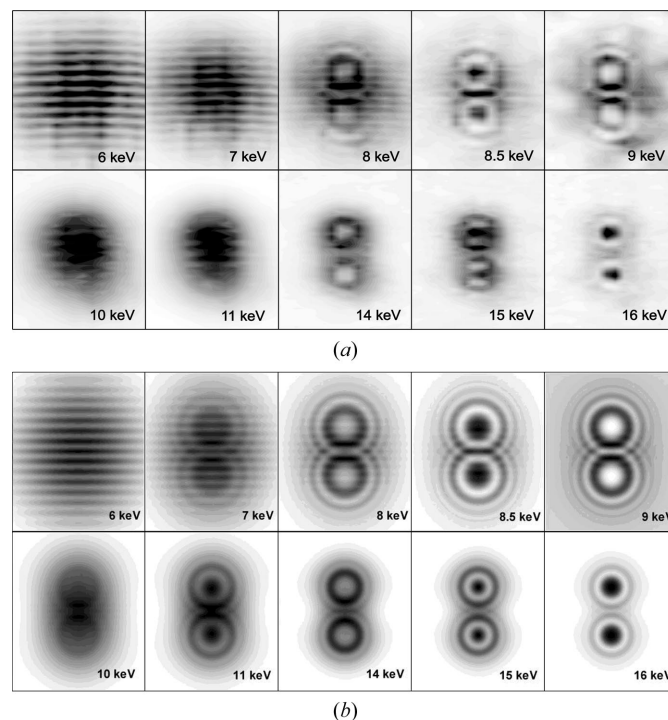


Figure 8
Two-dimensional intensity maps of the interference pattern at ten energy values. Double pinhole: 37 μm separation and vertical orientation. The 900 data points were recorded within an area of $100 \mu\text{m} \times 120 \mu\text{m}$ (horizontal \times vertical). (a) Experiment. (b) Simulation, same dimension as in (a).

model function (1) to the experimental data using a least-squares method. The pinhole distance and the diameter were also determined by this fit. Some typical normalized diffraction patterns of the 11 μm vertically separated pinholes are shown in Fig. 9, together with the results of the best fit.

The experiment was repeated with horizontally aligned pinholes. By performing horizontal detector scans, similar diffraction patterns were obtained. The measured fringe visibilities of both experiments are shown as a function of energy in Fig. 10. For the experiment with vertical and horizontal pinhole alignment the same pair of pinholes was used. The effective pinhole parameters were determined from the mean values which were calculated from several diffraction profiles at different energies. The determined pinhole diameter varies slightly with energy because the pinholes are slightly conical. This is the reason why the determined effective pinhole diameter is somewhat smaller for lower energies than for higher energies. The calculated pinhole parameters are: vertically, $d_v = 2.6 \pm 0.1 \mu\text{m}$, $D_v = 12.6 \pm 0.1 \mu\text{m}$, and, horizontally, $d_h = 2.6 \pm 0.1 \mu\text{m}$, $D_h = 12.8 \pm 0.1 \mu\text{m}$. These values are about 15% larger than those determined using electron microscopy. One reason might be the fact that the mathe-

tical model of Fraunhofer diffraction is a rough approximation for the present experiment.

In order to obtain more precise numerical values of the visibility, despite the small detector distance and the large detector pinhole, further calculations were necessary. The diffraction curves calculated with the fitting parameters were numerically deconvoluted with a slit function of width 2.5 μm for vertical pinhole alignment and 5 μm for the horizontal measurements taking into account the reduction of the pinhole size mentioned above.

The fringe visibility is increased after deconvolution, mostly at small fringe distance (high energy values). These corrected visibility values agree with the results of numerical simulations using Fresnel diffraction theory. Fig. 10 shows the visibility for the two experiments as a function of energy before and after deconvolution. From the visibility data an effective or virtual size s of the X-ray source was calculated using equation (2). The solid curves in Fig. 10 were obtained as a result of the best fit of experimental visibility to equation (2). A constant value of s within the observed energy range was assumed. An effective source size of 116 $\mu\text{m} \times 145 \mu\text{m}$ (vertical \times horizontal) is quite large compared with the vertical source size of about 50 μm at the BESSY II synchrotron obtained with a pinhole camera (Holdack *et al.*, 2001).

The reduction of fringe contrast in the experiment could be caused by small instabilities in the position of the X-ray source during the experiment. The possibilities of eliminating such oscillations with our experimental set-up were quite low. The time resolution of our experiment is limited to several minutes by the measuring time per data point and the number of data points which were necessary for measuring a single interference fringe. Oscillations with higher frequencies give a smearing of the intensity distribution and finally a reduction of the measured fringe visibility.

As seen in Fig. 8(a), the Young's fringes are not completely straight lines over the whole image width. This may be interpreted as a result

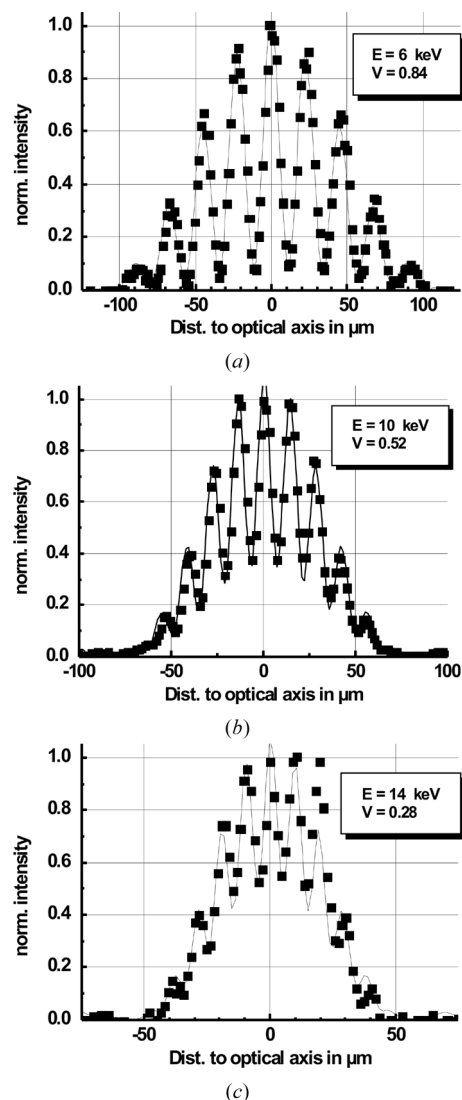


Figure 9
Measured interference fringes with the double pinhole for 6, 10 and 14 keV radiation. The squares show the measured data extracted from the data set shown in Fig. 6, and the solid lines are the result of a best fit of equation (1).

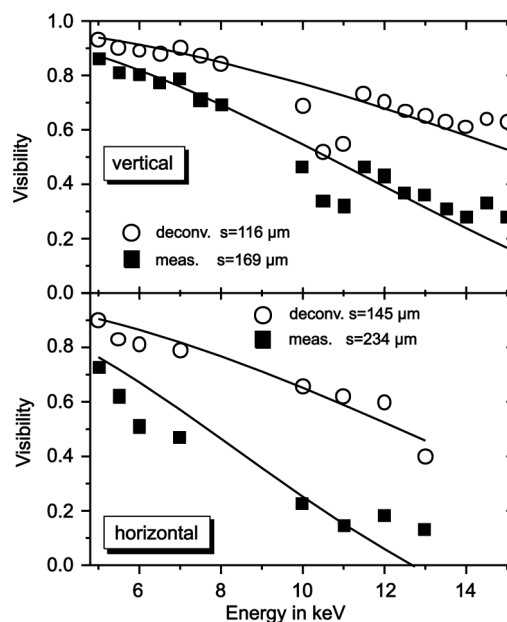


Figure 10
Visibility of the interference fringes as a function of energy for vertical and horizontal pinhole separation. The values calculated from the measured data are shown, together with the values obtained after deconvolution with a slit function. The solid lines are the result of a best fit to equation (2) for determination of the effective size of the X-ray source s .

of the movement of the source point during the measurement (the detector scans were performed in the vertical direction).

Another reason for observing much lower fringe contrast than expected for a source size of about 50 μm could be a non-polished Be window (Snigirev *et al.*, 1996). The UHV exit window at about 0.5 m in front of the double pinhole probably deforms and modifies the incident plane wavefront and partially destroys the good coherence properties of the incident beam. Its influence will be quantitatively investigated after replacement by a polished window. The measurements were repeated a few times at different positions of the Be window in order to find local fluctuations of the visibility, but no significant differences between the interference patterns could be found.

Following Robinson *et al.* (2003), the scattering of X-rays at a Be window at about 8 m before the double pinhole causes decoherence and forms a secondary X-ray source. The unexpected small values of the visibility could be explained by this much lower source distance. The present visibility data are consistent with studies of the visibility of diffraction rings of small circular apertures (Panzner *et al.*, 2004). An exact experimental investigation of the decoherence effects is in progress.

3.5. Point diffraction interferometer (PDI)

In a PDI the incident wave is divided into two coherent waves by a partially transmitting foil containing a single pinhole. The wave diffracted by the pinhole produces a spherical reference wavefront that interferes with the attenuated wavefront transmitted by the metal foil. Besides the loss of intensity by absorption, the transparent metal foil introduces an optical path-length difference between the spherical wave and the plane reference wave (see Fig. 2c). Owing to the variable refraction index the relative phase of both coherent wavefronts is a function of wavelength.

The interference pattern of a PDI is an in-line hologram of a small source point (Fresnel zone plate). For observation of high-contrast interference fringes the amplitudes of both waves have to be almost equal. The interference pattern in the detector plane are concentric

bright and dark rings around the optical axis and can be treated more or less independently if the two pinholes in the mask are sufficiently separated and the overlap of the two spherical waves in the observation plane is small.

An energy spectrum measured at the optical axis behind a single pinhole is discussed quantitatively in the following. The spectrum gives the intensity of the zeroth Fresnel zone of the interferogram as a function of energy (see Fig. 11). It has already been shown as a horizontal line crossing the apices of the parabola-like pattern on the right-hand side of Fig. 7. The intensity oscillations are mainly caused by the variable optical path-length difference introduced by the metal foil, but for lower energies mainly by the double-pinhole interference.

The optical path-length difference Δt between a wave passing through a foil of thickness t_0 with a refraction index $n = 1 - \delta - i\beta$ and a wave passing through a pinhole is given by $\Delta t = t_0\delta$. The phase shift can be written as $\Delta\varphi = \Delta t 2\pi/\lambda$ (δ and β are the real and imaginary parts of the refraction decrement). In an 'on-axis' spectrum we expect an intensity maximum for constructive interference at a phase shift of $\Delta\varphi = 2N\pi$ (where N is an integer) and a minimum intensity for $\Delta\varphi = (2N + 1)\pi$. From the positions of the intensity minimum and maximum in Fig. 11 we find immediately the sequence of energy values where the phase shift introduced by the metal foil is a multiple integer of π . The value of N , the so-called phase offset, cannot be measured directly by this experiment but was determined by calculations of the total phase shift from tabulated data (Henke *et al.*, 1993), assuming a tantalum foil with $t = 30 \mu\text{m}$ according to the specifications of the supplier. The measured and the calculated values for the refraction index decrement are shown in Fig. 12 as a function of energy and both data coincide quite well.

For more precise experimental results with the PDI, at least one of the thickness of the foil or its refraction index decrement has to be known exactly in order to calculate the other quantity. The uncertainty in both might cause the small discrepancies between experiment and theory in our case. For instance, a thickness of $t = 29 \mu\text{m}$ gives a much better agreement between experiment and theory.

The value of the spectral refraction index decrement δ can be obtained in a wide energy range using the expression $\delta = \Delta\varphi\lambda/(2\pi t_0)$. Taking again $t_0 = 30 \mu\text{m}$ we obtain the second data set shown in Fig. 12 together with theoretical data. A measurement of δ near to the

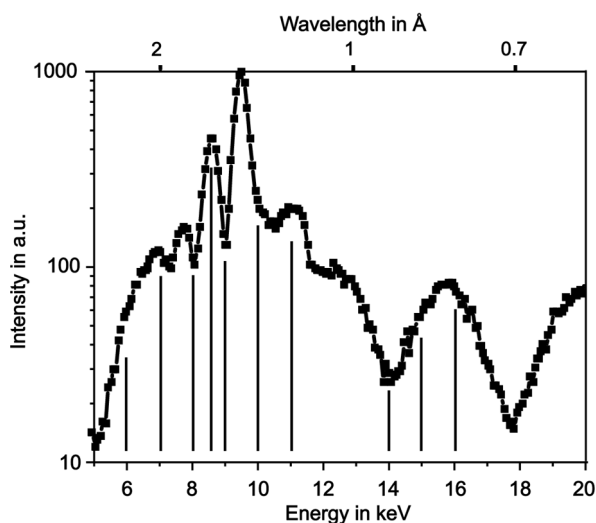


Figure 11 Energy spectrum measured on the optical axis ($x = 0$) behind a pinhole (see Fig. 7) giving the intensity of the zeroth Fresnel zone as a function of energy. The intensity oscillations are caused by the energy-dependent phase shift of the metal foil. The vertical lines correspond to the energy values of the area maps in Fig. 8.

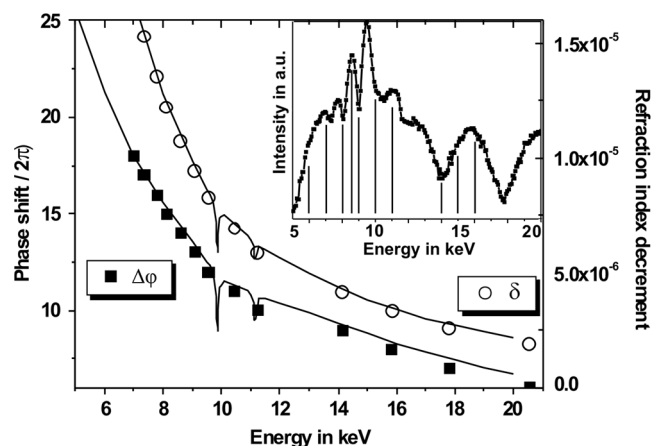


Figure 12 Phase shift $\Delta\varphi$ (including an offset correction) between the diffracted and transmitted wave for a PDI of 30 μm tantalum foil as a function of energy. The values were determined from the position of the interference minima and maxima in the on-axis energy spectrum of Fig. 11. The decrement of the refraction index, δ , is shown on the right-hand axis. Symbols signify the measured values and solid lines are based on calculations.

absorption edges (small dips at 10 and 11 keV) requires a more accurate measurement. In this case a certain interference maximum could be shifted to a well defined energy by changing the effective thickness of the foil by rotation around an axis parallel to the foil surface. Of course, high-resolution measurements are also limited by the energy resolution of the detector but can also be performed using tunable monochromatic radiation.

Finally, the accuracy of the experimental determination of the phase shift using the energy values of the interference minima and maxima is not very high, especially in the case of low transmission where the interference of both pinholes contributes to the measured intensity. Nevertheless, we could show the possibility of such kinds of measurements which can, of course, be performed more precisely using a single pinhole in the foil.

The presented phase-shift measurement for X-rays using a PDI is relatively insensitive to mechanical vibrations compared with single-crystal interferometers. The in-line geometry allows an easy alignment and even phase-shifting interferometry might be possible by a tiny rotation of the metal foil.

4. Conclusion

Two types of interferometer for hard X-rays have been realised and investigated with incident white synchrotron radiation using an energy-dispersive detector with an energy resolution of about 200 eV. In both interferometers a thin tantalum foil containing small pinholes was used as a beamsplitter. In the case of low energy and high absorption a double-pinhole interferometer was realised and Young's interference fringes were used to determine the coherence properties of the incident radiation in a spectral range from 5 to 15 keV. In the low-absorbing part of the X-ray spectrum (high energy) the typical interference effects of a point diffraction interferometer were observed. The phase shift of the Ta membrane was determined in a wide energy range as a function of energy. After solving the problem of the generation of micropinholes in thicker metal foil ($t > 50 \mu\text{m}$), DPI experiments with lower background owing to transmission will be possible in a much wider spectral range. In parallel with the experiments reported here, static speckles in reflection geometry have been observed over a wide spectral range using a similar experimental set-up (Panzner *et al.*, 2003). The photon flux is sufficient for performing future experiments on the second time scale at the same beamline.

We could show that X-ray interferometry using white synchrotron radiation together with an energy-dispersive detector is a useful supplement to monochromatic- or pink-beam experiments. With the improvement of energy-dispersive detectors in terms of energy resolution and maximum count rate, the field of its applications in X-ray physics will increase.

The authors would like to thank U. Pietsch, J. Grenzer, A. Pucher and T. Panzner (Universität Potsdam) for providing a well prepared beamline and for fruitful discussions. S. M. Kuznetsov (ESRF, Grenoble) is acknowledged for providing software for numerical simulations. Max-Planck-Institute for Colloids and Interfaces (Potsdam, Golm), the BESSY GmbH (Berlin) and the Hahn-Meitner-Institute (Berlin) are kindly acknowledged for financial support for beamline instrumentation.

References

- Bodenthin, Y., Grenzer, J., Lauter, R., Pietsch, U., Lehmann, P., Kurth, D. G. & Möhwald, H. (2002). *J. Synchrotron Rad.* **9**, 206–209.
- Born, M. & Wolf, E. (1999). *Principles of Optics*. Cambridge University Press.
- Burge, R. E., Yuan, X. C., Slark, G. E., Browne, M. T., Charalambous, P., Lewis, C. L. S., Cairns, G. F., MacPhee, A. G. & Neely, D. (1999). *Opt. Commun.* **169**, 123–133.
- Chang, C., Naulleau, P., Anderson, E. & Attwood, D. (2000). *Opt. Commun.* **182**, 25–34.
- Cloetens, P., Barret, R., Baruchel, J., Guigay, J.-P. & Schlenker, M. (1996). *J. Phys. D*, **29**, 133–146.
- David, C., Musil, C., Souvorov, A. & Kaulich, B. (2000). *X-ray Microscopy*, edited by W. Meyer-Ilse, T. Warwick and D. Attwood, pp. 704–707. Berkeley: AIP.
- Ditmire, T., Gumbrell, E. T., Smith, R. A., Tisch, J. W. G., Meyerhofer, D. D. & Hutchinson, M. H. R. (1996). *Phys. Rev. Lett.* **77**, 4756–4759.
- Francon, M. (1966). *Optical Interferometry*. New York/London: Academic Press.
- García-Sucerquia, J. I., Castaneda, R., Medina, F. F. & Matteucci, G. (2001). *Opt. Commun.* **200**, 15–22.
- Goldberg, K. A., Beguiristain, B., Bokor, J., Medeck, H., Attwood, D. T., Jackson, K., Tejnil, E. & Sommargren, G. E. (1995). *J. Vac. Sci. Technol. B*, **13**, 2923–2927.
- Goodman, J. W. (1968). *Introduction to Fourier Optics*. San Francisco: McGraw-Hill.
- Henke, B. L., Gullikson, E. M. & Davis, J. C. (1993). *Atom. Data Nucl. Data Tables*, **54**, 181–343. (http://www-cxro.lbl.gov/optical_constants/.)
- Holladack, K., Feikes, J. & Peatman, W. B. (2001). *Nucl. Instrum. Methods, A467/A468*, 235.
- Ishikawa, T. (1988). *Acta Cryst.* **A44**, 496–499.
- Kohn, V., Snigireva, I. & Snigirev, A. (2000). *Phys. Rev. Lett.* **85**, 2745–2748.
- Lang, A. R. & Makepeace, A. P. W. (1999). *J. Synchrotron Rad.* **6**, 59–61.
- Leitenberger, W., Kuznetsov, S. M. & Snigirev, A. (2001). *Opt. Commun.* **191**, 91–96.
- Leitenberger, W. & Snigirev, A. (2001). *J. Appl. Phys.* **90**, 538–544.
- Leitenberger, W., Weitkamp, T., Drakopoulos, M., Snigireva, I. & Snigirev, A. (2000). *Opt. Commun.* **180**, 233–238.
- Leitenberger, W., Wendrock, H., Bischoff, L., Panzner, T., Pietsch, U., Grenzer, J. & Pucher, A. (2003). *Physica B*, **336**, 63–67.
- Lengeler, B. (2001). *Naturwissenschaften*, **88**, 249–260.
- Lengeler, B., Schroer, C. G., Benner, B., Gunzler, T. F., Kuhlmann, M., Tummeler, J., Simionovici, A. S., Drakopoulos, M., Snigirev, A. & Snigireva, I. (2001). *Nucl. Instrum. Methods, A467*, 944–950.
- Linnik, W. (1933). *Proc. Acad. Sci. USSR*, **1**, 208–211.
- Liu, Y., Seminario, M., Tomasel, F. G., Tomasel, F. G., Chang, C., Rocca, J. J. & Attwood, D. T. (2001). *Phys. Rev. A*, **63**, 033802.
- Naulleau, P. P. & Goldberg, K. A. (1999). *Appl. Opt.* **38**, 3523–3532.
- Neissendorfer, F. U. P., Brezesinski, G. & Mohwald, H. (1999). *Meas. Sci. Technol.* **10**, 354–361.
- Panzner, T., Leitenberger, W., Grenzer, J. & Pietsch, U. (2003). *J. Phys. D*, pp. A93–A97.
- Panzner, T., Leitenberger, W., Grenzer, J. & Pietsch, U. (2004). In preparation.
- Paterson, D., Allman, B. E., McMahon, P. J., Lin, J., Moldovan, N., Nugent, K. A., McNulty, I., Chantler, C. T., Retsch, C. C., Irving, T. H. K. & Mancini, D. C. (2001). *Opt. Commun.* **195**, 79–84.
- Robinson, I. K., Kenny-Benson, C. A. & Vartanyants, I. A. (2003). *Physica B*, **336**, 56–62.
- Smartt, R. N. & Steel, W. H. (1975). *Jpn. J. Appl. Phys. Suppl.* **14**, 351.
- Snigirev, A., Kohn, V., Snigireva, I. & Lengeler, B. (1996). *Nature (London)*, **384**, 49–51.
- Snigirev, A., Snigireva, I., Kohn, V. G. & Kuznetsov, S. M. (1996). *Nucl. Instrum. Methods, A370*, 634–640.
- Takayama, Y., Tai, R. Z., Hatano, T., Miyahara, T., Okamoto, W. & Kagoshima, Y. (1998). *J. Synchrotron Rad.* **5**, 456–458.
- Thompson, B. J. & Wolf, E. (1957). *J. Opt. Soc. Am.* **47**, 895.
- Walker, J. F., Moore, D. F. & Whitney, J. T. (1996). *Microelec. Eng.* **30**, 517.
- Weitkamp, T. (2002). PhD thesis, Universität Hamburg, Germany.
- Weitkamp, T., Rau, C., Snigirev, A., Benner, B., Günzler, T. F., Kuhlmann, M. & Schroer, C. G. (2002). *Proc. SPIE*, **4503**, 92–102.
- Wilkins, S. W., Gureyev, T. E., Gao, D., Pogany, A. & Stevenson, A. W. (1996). *Nature (London)*, **384**, 335–338.
- Yabashi, M., Tamasaku, K. & Ishikawa, T. (2001). *Phys. Rev. Lett.* **87**, 140801-1–140801-4.
- Young, T. (1807). *Lect. Nat. Philos. I*, p. 464.